

Model testing of the spatial–temporal evolution of a landslide failure

Junwei Ma^{1,2,3} · Huiming Tang^{1,3} · Xinli Hu³ · Antonio Bobet² · Rui Yong⁴ · Mutasim A. M. Ez Eldin³

Received: 6 August 2015 / Accepted: 7 April 2016 / Published online: 21 April 2016
© Springer-Verlag Berlin Heidelberg 2016

Abstract This paper outlines the spatial–temporal evolution of a landslide. A multiple monitoring system that consists of a three-dimensional (3D) laser scanner, a particle image velocimeter (PIV), earth pressure cells (PCs), and a thermal infrared (TIR) imager were designed and employed for a 1 g landslide model case study. The displacement, velocity, lateral earth pressure and surface temperature were recorded during the evolution of a landslide. Four stages of evolution were identified using the measured displacements: the initial stage, the uniform stage, the accelerated stage and the failure stage. The deformation, lateral earth pressure and surface temperature of a landslide were monitored during each stage. The distribution of the lateral force with depth varied significantly during movement, and the depth of the maximum soil pressure increased with movement. The surface temperature of the moving mass was significantly higher than the surface temperature of the nonmoving mass. The average change in surface temperature showed a significant increase in surface temperature followed by a decrease in surface temperature prior to failure. This study provides

procedures and solutions for landslide monitoring, interpreting landslide initiation and detecting landslides.

Keywords Landslide model test · Spatial–temporal evolution · Deformation · Lateral soil pressure · Surface temperature

Introduction

A landslide is a process that occurs on temporal and spatial scales and may involve progressive deformation of a sliding body, propagation and extension of surface fissures, and eventual failure. Studies of landslide evolution can serve as the foundation for the assessment of landslide risk and the prediction of runout and time of failure, as well as early warning systems (Gokceoglu and Sezer 2009).

Studies of the evolution of landslides are generally based on measurements from in situ instrumentation, such as conventional topographic surveys, global positioning systems (GPSs), extensometers, piezometers and inclinometers. For example, extensometers provide continuous data of movement; piezometers measure groundwater pore pressure; and inclinometers provide the rate and direction, with depth, of the landslide deformation and the thickness of the sliding zone (Angeli et al. 2000; Corominas et al. 2000; Corsini et al. 2005).

Measurements are usually collected at selected locations in the landslide (e.g., landslide crown, depletion zone, and accumulation zone), which may not be representative of an entire unstable area (Casagli et al. 2010; Tarchi et al. 2003). An area-sensing approach that enables the collection of detailed and spatially extensive information does not have this limitation. For example, aerial photography, photogrammetric techniques and Synthetic Aperture Radar

✉ Huiming Tang
hmtang6205@sina.com; tanghm@cug.edu.cn

¹ Three Gorges Research Center for Geo-hazards of Ministry of Education, China University of Geosciences, Wuhan 430074, Hubei, People's Republic of China

² School of Civil Engineering, Purdue University, West Lafayette, IN 47907, USA

³ Faculty of Engineering, China University of Geosciences, Wuhan 430074, Hubei, People's Republic of China

⁴ Shaoxing University, Shaoxing 312000, Zhejiang, People's Republic of China

(SAR) interferometry have been successfully employed to document the evolution of landslides over time (Casson et al. 2003; Squarzonni et al. 2003; Strozzi et al. 2005; van Westen and Lulie Getahun 2003; Walstra et al. 2004).

Model testing in the laboratory is an effective tool that has an important role to play in landslide engineering. Although it is task-intensive, model testing, i.e., small-scale testing, has proven instrumental for improving our understanding of landslide mechanisms and processes (Iverson 2015). This approach has been applied extensively to investigating the characteristics, stability, and evolution of landslides (Jia et al. 2009; Lin and Wang 2006; Moriwaki et al. 2004; Ochiai et al. 2004; Rianna et al. 2014). Technical literature supports the notion that similarities between laboratory results and field observations can be obtained using the principle of similarity (Cheng and Luo 2010; Fan et al. 2009; Luo et al. 2010). Due to its effectiveness, the similarity approach has been employed extensively to investigate the fundamental principles of landslide movement (Cheng and Luo 2010; Feng et al. 2015; Luo et al. 2010; Tang et al. 2014a; Zhang et al. 2009).

Most studies, however, have focused on a single parameter that may provide only a limited viewpoint of the complexity of the phenomena, which is better characterized with multiple parameters. Acquiring multiple types of parameters is essential for a complete understanding of the mechanisms of landslide failure (Sun et al. 2014). A successful example of the use of complex, overlapping monitoring systems is the Huangtupo landslide, which was monitored using the world's first three-dimensional (3D) multi-field monitoring system to assess its stability (Tang et al. 2014b). As another example, the Majiagou landslide was instrumented with distributed fiber optic sensing (DFOS) to better understand the dynamics, characteristics, and evolution of a landslide mass (Sun et al. 2014).

In this study, a 1-g landslide model test was conducted to relate landslide deformation with multiple systems of monitoring data. The information included deformation, lateral soil pressure and surface infrared radiation temperature data, which were obtained over the entire model test area via a multiple-monitoring system that consisted of a 3D laser scanner, a particle image velocimeter (PIV), earth pressure cells (PCs) and a thermal infrared (TIR) imager. Analyses were performed based on the measurements that were collected during the model test. Four stages of evolution (i.e., initial, uniform, accelerated and failure) were distinguished from the measured displacements. The evolution of the deformation, lateral force and surface temperature were investigated during each stage of evolution. Note that the objective of the study was to use the Majiagou landslide as a reference to investigate the use of area-extensive multiple complementary measurement systems

for landslide monitoring. The scope of the study did not involve duplicating or modeling the actual landslide, which would have been difficult due to the complexities and history of the Majiagou landslide.

Description of the landslide model test

The prototype that was selected for this study was the Majiagou #1 landslide. This landslide is located on the left bank of the Zhaxi River, which is a tributary of the Yangtze River, approximately 5 km northwest of Guizhou Town of Zigui County in Hubei Province (Fig. 1).

The landslide occurred at a site that is characterized by basement rock that consists of Jurassic sandstone interbedded with silty sandstone (Ma et al. 2016). The material of the sliding mass is described as a gravelly soil mixed with silty clay, and the sliding zone consists of weathered silty mudstone. The landslide extends over a horizontal distance of 538 m between the following elevations: 280 m at the crown and 135 m at the toe. The average slope is 15°; the slope is steepest in the lower portion, gentle in the middle, and steep in the upper slope.

The law of similitude was applied to reproduce some of the field processes in the laboratory. The landslide model was similar to the prototype in terms of geometry, material properties, initial state, and boundary conditions. The law of similitude that was applied to the 1 g landslide test was based on the work of Iai (1989). This approach simplifies the need for scaling parameters in the 1 g model test (Lin and Wang 2006; Wang and Lin 2011). The scaling parameters between the prototype and model were derived according to the Buckingham π theorem (Bridgman 1922). The results are listed in Table 1; λ is the scaling ratio between the prototype and the model and is represented as $\lambda = 40$ in this study.

The width and length of the model, which was placed in a rigid steel box, were 0.9 and 2.0 m, respectively. The box had a transparent side composed of thick acrylic to enable visual observation of the deformation and movement along the failure surface (Figs. 2, 3). The height of the back slope, which had a base layer that was composed of masonry to simulate the bedrock, was 0.74 m (Tang et al. 2014a). A 4-cm-thick sliding layer was placed on the top surface of the masonry. The layer had three segments at different inclinations: a 71-cm-long segment that dipped 15°, a 53-cm-long segment that dipped 24°, and a 52-cm-long segment that inclined upwards at 16° (Fig. 3).

The model soils for the matrix and the sliding layer were identical to the soils employed in previous studies; the relevant information is presented in Tang et al. (2014a). The soils were composed of a mixture of clay, sand, bentonite and water, with mass proportions of 49.1:39:0.9:11

Fig. 1 **a** Location of the Majiagou landslide in the Three Gorges Reservoir area, Hubei Province, China. **b** Photograph of the Majiagou landslide (the landslide boundary is illustrated with dashed red lines)

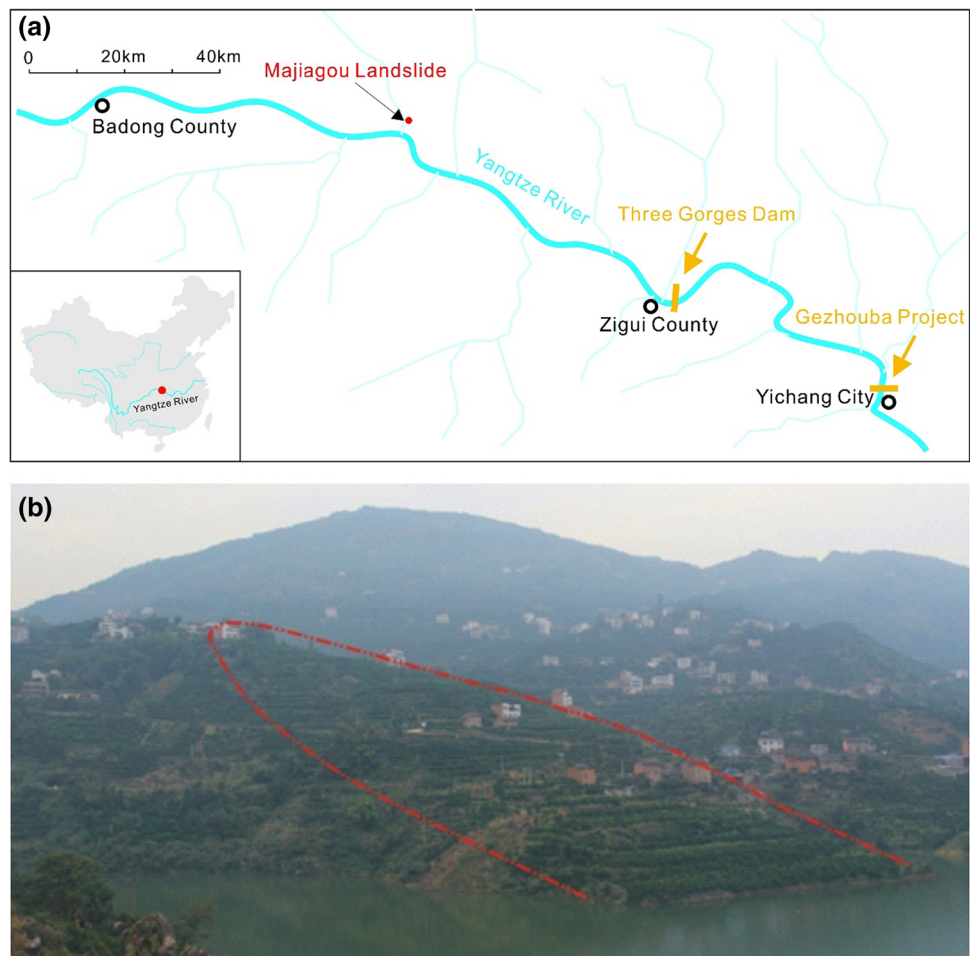


Table 1 Law of similitude for the prototype and the model

Term	Scaling factor	Term	Scaling factor
Length (L)	λ	Gravity (g)	1
Mass density (ρ)	1	Cohesion (c)	λ
Friction angle (φ)	1	Elastic modulus (E)	λ
Permeability coefficient (k)	$\lambda^{1/2}$		

A scaling factor of $\lambda = 40$ was used in the model test

(clay:sand:bentonite:water), which formed a stiff material that simulated the properties of the sliding mass. A mixture of clay, glass beads and water in proportions of 32:60:8 by mass was employed to simulate the soft materials that formed the sliding layer. The clay that was employed in the test originated in the Majiagou landslide. The following procedures were conducted to obtain homogeneous materials prior to mixing. The soil was air-dried, disaggregated with a crusher, and screened through a 2-mm mesh. A concrete mixer was used to prepare the model soil and obtain a uniform water content distribution. To obtain a uniform soil sample during compaction, the soil was placed in a series of 15-cm layers that were parallel to the base of

the model and compacted by tamping with a rubber hammer that was dropped 160 times per layer. After placement, the soil was trimmed manually to obtain the desired shape. The model slope after construction is shown in Fig. 2.

The material properties of the prototype and the model that were determined from direct shear, uniaxial compression and permeability tests are listed in Table 2. The mass density, internal friction angle, and permeability of the mass, as well as the Young’s modulus of the sliding zone, are consistent with the theoretical scaling factors. However, important differences between the cohesion of the prototype and the model are attributed to the difficulty in obtaining the small values that are required via the

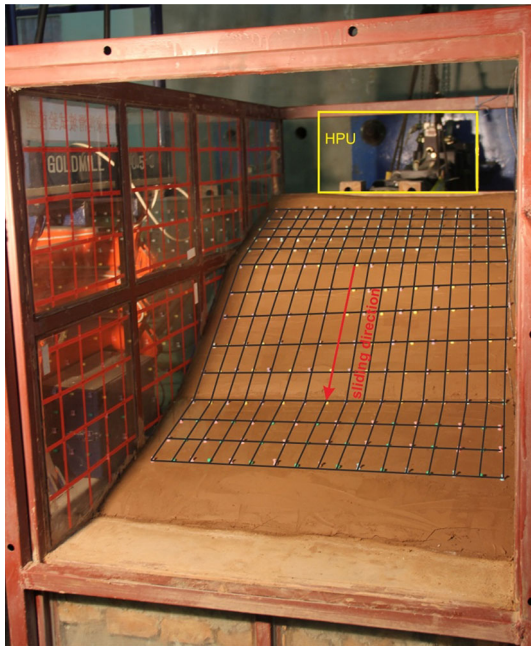


Fig. 2 Overview of the slope model after construction

scaling process. Because the objective of this study was the development and assessment of a multi-measurement system for landslides, instead of duplication of the actual landslide failure, the differences in strength between the model and the field were not considered to be critical.

The driving load was imposed at the top of the model, as shown in Fig. 3, through a hydraulic power unit (HPU) with a load precision of 0.5 % that was attached to a

concrete reaction wall. The load was recorded by the HPU's electrical controller. To approximate the stop-slide type of movement that was observed in the landslide (Tang et al. 2014a), a series of ramp and hold load steps was applied. The magnitude of the force in each step was calculated using limit equilibrium and the similitude law (Tang et al. 2014a). The first step consisted of a load of 250 N. In the second step, which lasted 20 min., the load was increased to 200 N and maintained for 40 min. Several identical steps followed until large deformations appeared in the model and failure occurred; refer to Fig. 5.

The monitoring system consisted of a high-speed multi-channel data acquisition apparatus (DT80G), a HPU (Model 505.60), a 3D laser scanner (RIEGL VZ-400), a video camera, an earth PC (Model XTR-2030) and a TIR imager (Model FLIR SC660 with a temperature sensitivity of 0.03 °C), as shown in Fig. 3.

Surface movements were continuously recorded with the video camera and the 3D laser scanner (Fig. 3). The surface infrared radiation temperature was measured using the TIR camera, which was located slightly above the landslide surface (Fig. 3). Fifteen earth PCs with a measurement range of 0–500 kPa were installed at different depths to monitor the soil pressure (Figs. 3, 4). The earth PCs in the upslope region were placed at depths of 6, 12, 18, 24, and 30 cm below the surface (PC1). In the middle slope region, the earth PCs were installed at depths of 5, 10, 15, 20, 25 and 30 cm (PC2). In the downslope region, four soil PCs were embedded at depths of 7, 14, 21 and 28 cm (PC3) below the surface.

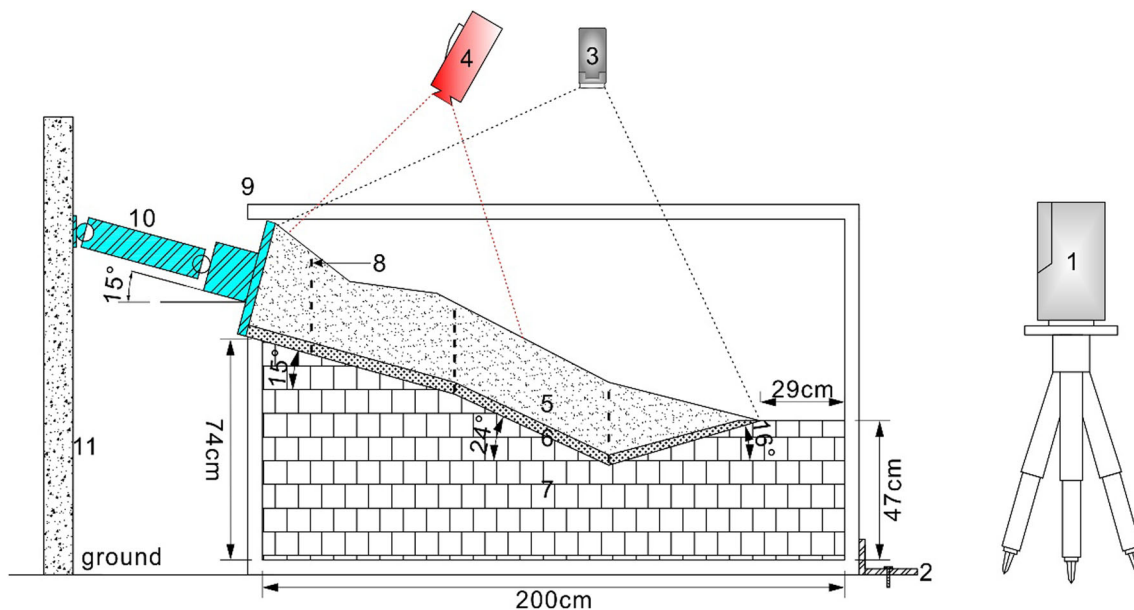


Fig. 3 Distribution and location of the instrumentation and equipment installed in the model. 1 3D laser scanner (RIEGL VZ-400); 2 reaction support; 3 video camera; 4 thermal infrared imager (FLIR

SC660); 5 sliding mass; 6 sliding zone; 7 bedrock; 8 earth pressure cell (PC, XTR-2030); 9 experiment enclosure; 10 hydraulic power unit (HPU, Model 505.60); 11 reaction wall

Table 2 Similarity relations between the prototype and the model landslide

Term	Prototype	Model
Mass density (kg/m ³)		
Sliding mass	21.14	19.2
Sliding zone	21.14	16.8
Cohesion (kPa)		
Sliding mass	–	11.2
Sliding zone	16–18	9.86
Friction angle (°)		
Sliding mass	–	18.91
Sliding zone	17–19	18.1
Elastic modulus (MPa)		
Sliding mass	300	2.4
Sliding zone	100	2.2
Permeability coefficient (<i>k</i>)		
Sliding mass	$(1.5\text{--}2.5) \times 10^{-4}$	3.25×10^{-5}
Sliding zone	–	2.02×10^{-5}

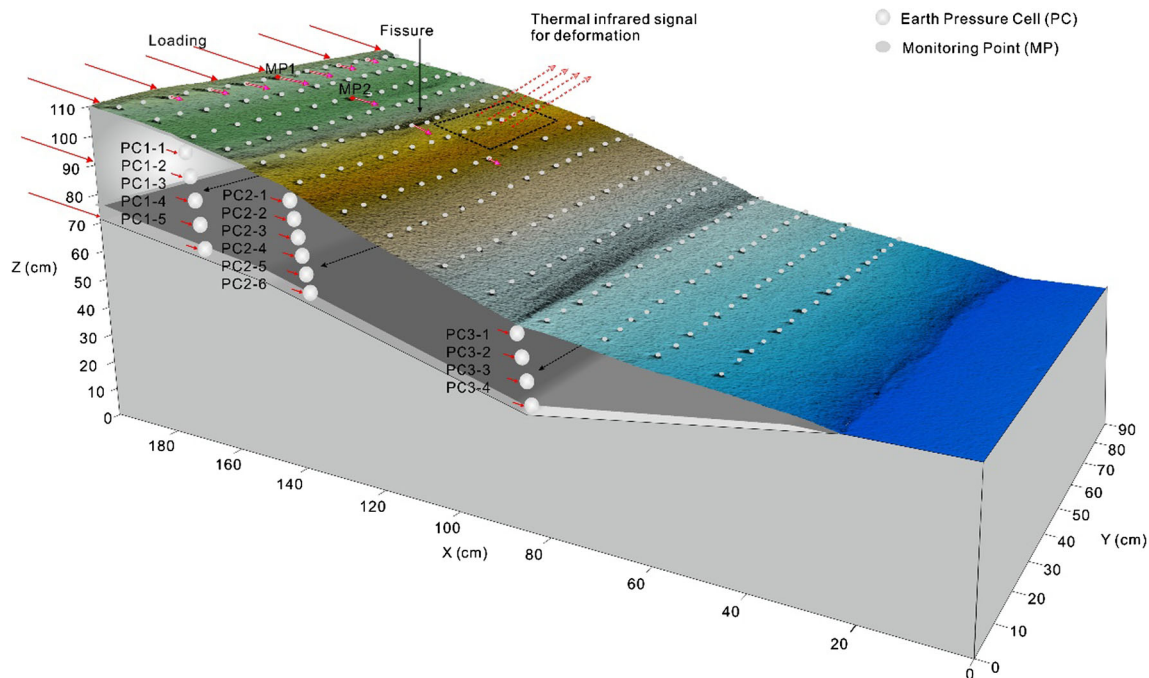


Fig. 4 Schematic of the model test. The location of the displacement monitoring points (MPs), earth pressure cells (PCs), and region where infrared radiation temperature was monitored (*dashed black rectangle*) are indicated. The surface elevations are shown with *color gradients*

3D laser scanning technology is useful for monitoring landslide deformation because it enables rapid collection of field topographical data with high accuracy and resolution (Abellán et al. 2006; Fanti et al. 2013; Jaboyedoff et al. 2012; Travelletti et al. 2008; Wang et al. 2013). Prior to loading, the surface was scanned to determine the undeformed, i.e., reference, shape of the mass. The deformations during the test were measured every 5 min. Spherical pushpins with a diameter of 1 cm were placed on the

surface as monitoring points (MPs) (Fig. 2) that can be identified as homonymic points using the IMAlign module of the Polyworks 10.0 software. The locations of the displacement MPs are shown in Figs. 2 and 4.

The deformation between reference points was determined using two methods: the benchmark method and the cloud-to-cloud comparison method (Abellán et al. 2010; Travelletti et al. 2008). In addition to the 3D laser scanner, a PIV was also employed to determine the surface velocity,

the local deformation and the particle motion. A PIV tracks pre-determined particles from two consecutive images using tracking algorithms, such as the Fourier transform and cross-correlation methods (Baba and Peth 2012; Wang and Lin 2011). The displacements were determined using the free PIV software PIVlab, version 1.35 (Thielicke and Stamhuis 2014).

Mechanically induced thermal effects have been extensively investigated (De Bruyn and Thimus 1996; Gischig et al. 2011a, b). Changes in the surface temperature of a material provide qualitative information for predicting fracture and failure (Wu et al. 2000, 2002, 2006a, b) and identifying landslides (Kusaka et al. 1993; Shikada et al. 1994).

Our model test was conducted on a rainy day (16 May 2013 in Wuhan, Hubei, China) to avoid scattering sunshine (Wu et al. 2006b). Access to the monitoring area was restricted, and the windows and curtains in the room were closed to eliminate environmental radiation effects (Wu et al. 2006b). The region where infrared temperature was monitored (dashed black rectangle) is indicated in Fig. 4. Six MPs within the area were selected as markers for thermal imaging before and during deformation. The initial surface temperature and the room temperature were recorded as references.

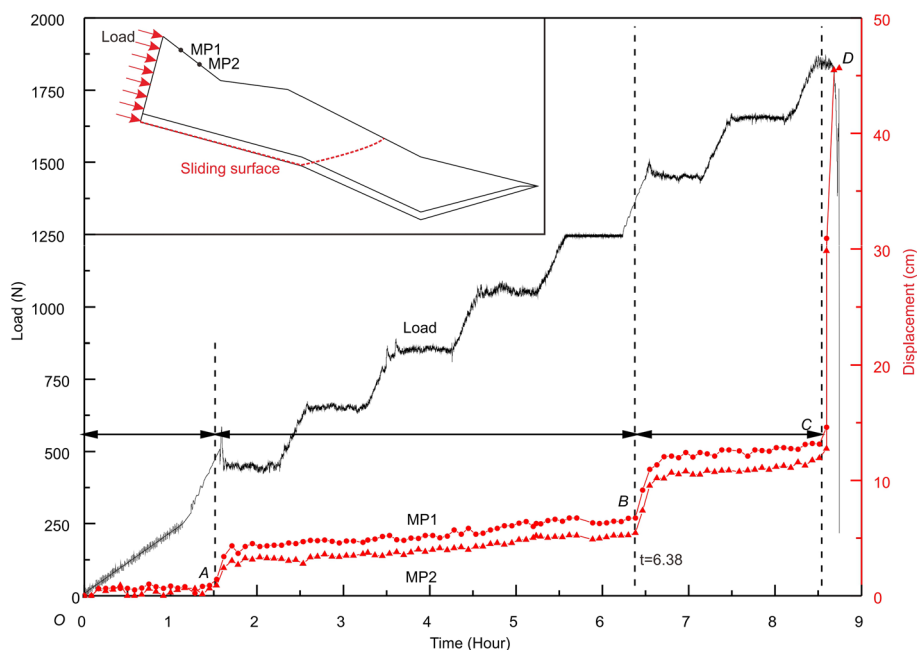
Spatial-temporal evolution of the landslide failure

The cumulative displacements at MP1 and MP2 and the applied force are shown in Fig. 5. Small deformations were detected at the beginning of the test; a deformation of

0.9 cm was attained at MP1 1.53 h after the beginning of the test. A significant movement was observed when the applied load increased to 485 N (point A in Fig. 5). The soil deformation gradually increased as the load increased. The cumulative displacement at MP1 increased to 6.7 cm at 6.38 h. Rapid soil movement occurred at a load of 1368 N (point B in Fig. 6). As the movement of the soil surface increased, a crack formed near the head of the slope (Fig. 4). The displacement at MP1 increased to 14.6 cm at 8.52 h (point C in Fig. 5). Rapid landslide failure occurred during the ninth loading stage at a peak load of 1,873 N (point D in Fig. 5). The sliding surface is shown in the inset of Fig. 5. Failure was characterized by a significant decrease in the magnitude of the load, whereas the displacement at MP1 significantly increased from 14.6 to 45 cm.

As shown in Fig. 6a, when a slip surface forms, the soil pressure near the slip surface decreases due to the soil movement (Fig. 6a). Thus, when the soil pressure decreased, a sliding surface was assumed to form. Figure 6b shows the displacement and soil pressure measured during the experiment by PCs 1–5 and 2–6. The stresses within the soil did not change significantly from the initial geostatic condition until the load increased to 485 N ($t = 1.53$ h in Fig. 6b). As the load applied to the soil mass increased, the surface deformation, which is shown at MP2 in Fig. 6b, and the pressures inside the landslide mass, which are shown for PCs 1–5 and 2–6 in Fig. 6b, increased. At PC 1–5, a pressure drop was observed at a depth of 30 cm at a load of 1368 N ($t = 6.38$ h after the beginning of the experiment). The pressure decreased steadily until

Fig. 5 Cumulative displacements measured at monitoring points MP1 and MP2 (the location of the monitoring points is shown in Fig. 4) with loading



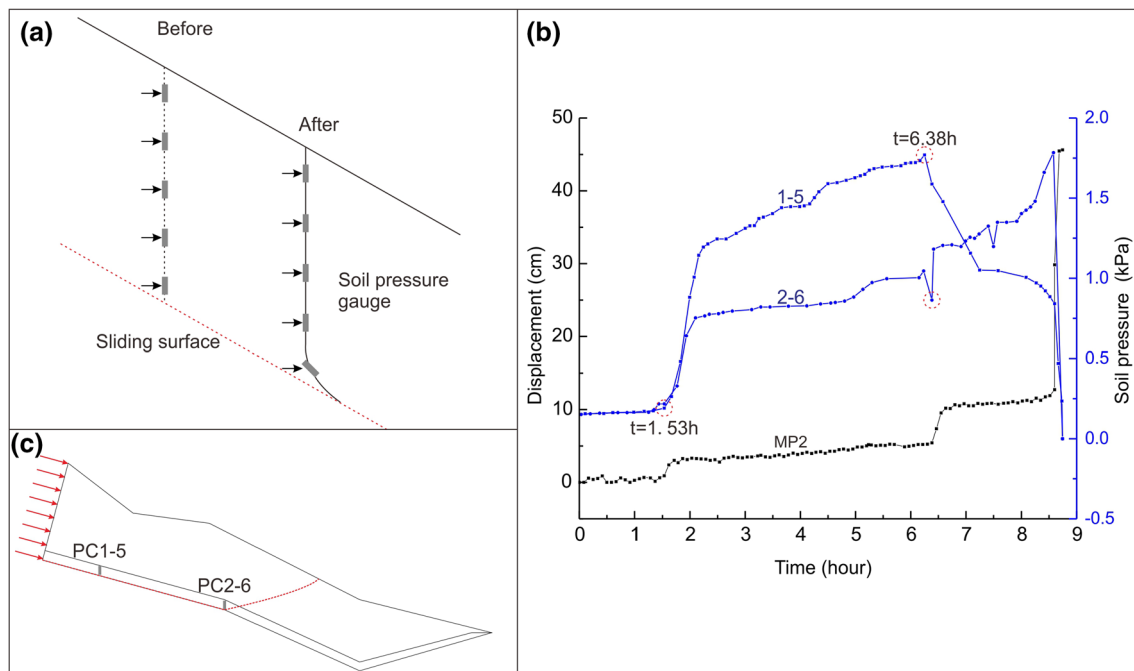


Fig. 6 **a** Detection of the sliding surface by a soil pressure gauge. **b** Measured soil pressure during the landslide. **c** Sliding surface observed in the test

failure; this result is interpreted as instability and slip at the location of PC 1–5 at a load of 1,368 N ($t = 6.38$ h). The soil pressure at PC 2–6 also showed a decrease, albeit transient, at the same load. The pressure at PC 2–6 continued to increase until failure. The delayed response of the two transducers indicates progressive failure of the landslide, which began in the uphill region and progressed downslope with additional loading. Global failure was associated with a significant decrease in the pressure that was registered in both transducers.

The evolution of the landslide was classified into the following four stages, based on the displacements (Tang et al. 2014a):

1. The initial deformation stage: from *O* to *A* in Fig. 5 (0–1.53 h; 0–485.22 N). During this stage, small deformations occurred (refer to measurements at MP1 and MP2), and no cracks on the surface were observed.
2. The uniform deformation stage: from *A* to *B* in Fig. 5 (1.53–6.38 h; 485.22–1367.93 N). The increasing load on the back of the model gradually produced noticeable soil pressures and displacements (Fig. 6b). A slight increase in the displacement rate (point *A* in Fig. 5) was observed at the end of the load ramp (485.22–586.5–457.89 N), with mean velocities of 3.2–7.2 cm/h between 1.53 and 1.71 h. Between 1.71 and 6.38 h (457.89–1367.93 N), the displacement continued to increase at approximately constant rates

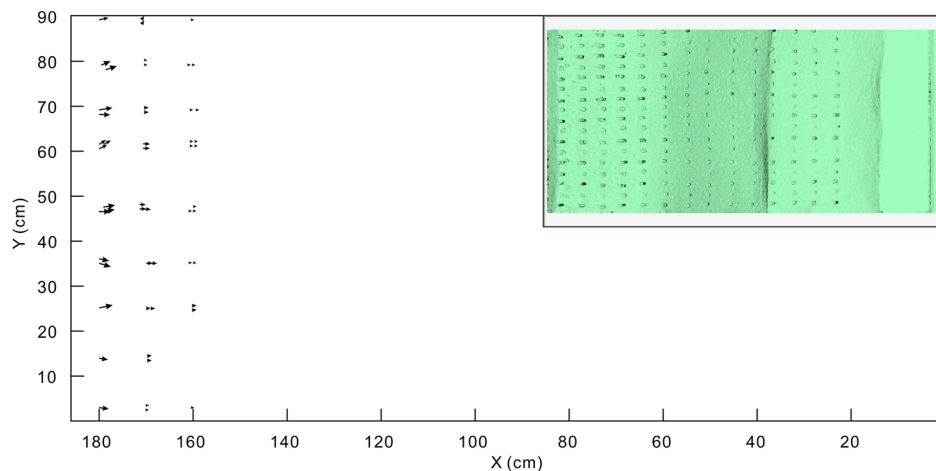
from 0.4 to 0.7 cm/h, irrespective of the load. This stage appears to be associated with soil creep. Intermittent cracks that were perpendicular to the sliding direction began to develop on the surface on the model. The locations of the cracks (fissures) are shown in Fig. 4.

3. The accelerated deformation stage: from *B* to *C* in Fig. 5 (6.38–8.52 h; 1367.93–1873.32 N). At the onset of this stage, the displacement significantly increased at rates of 9.4–11.6 cm/h between 6.38 and 6.72 h (1367.93–1452.32 N). The significant increase in displacement was likely caused by the previously described local failure and instability. The deformation subsequently and gradually increased at rates from 0.7 to 0.9 cm/h until the end of the stage; i.e., between 6.72 and 8.52 h (1452.32–1873.32 N). Note that the displacement rate was similar to the displacement rate of the preceding stage (the uniform deformation stage).
4. The failure deformation stage: from *C* to *D* in Fig. 5. The displacement substantially increased at rates of 76.4–141.8 cm/h, which denoted slip failure.

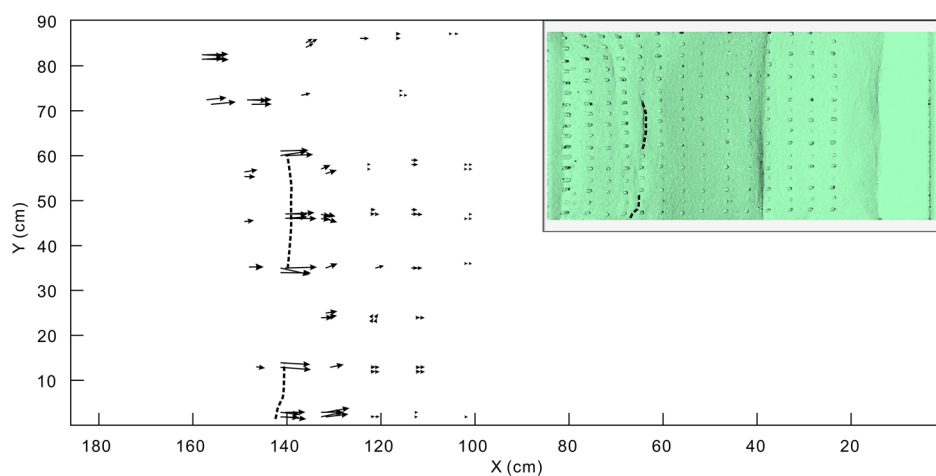
The PIV analysis was performed to obtain the velocities and directions of the particles on the slope surface. The results are shown in Fig. 7.

The PIV analysis results at the end of the initial deformation stage (0–485.22 N; 0–1.53 h) are shown in Fig. 7a. The velocity vectors were predominantly horizontal. Figure 7a shows a homogeneous pattern that indicates that the

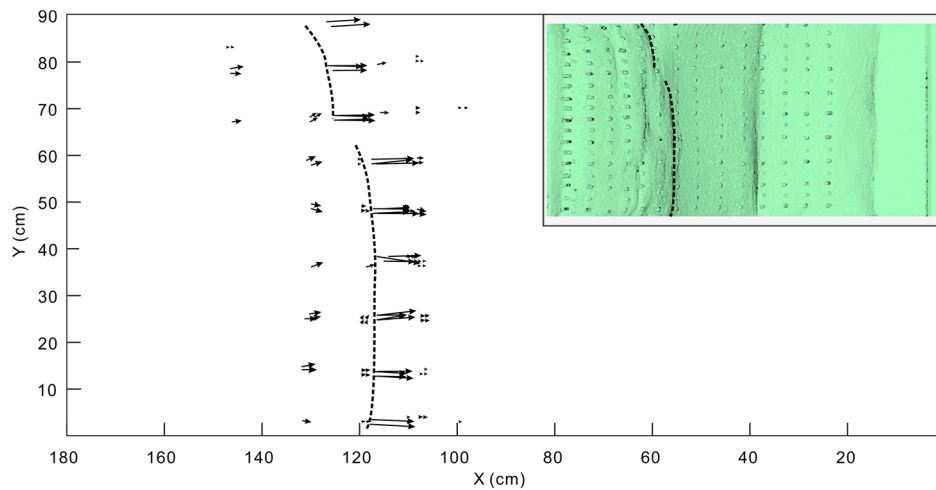
Fig. 7 Velocity vectors obtained from the PIV analysis and surface deformation (only every third vector is shown, and the vectors are magnified $6\times$). **a** At the end of the initial deformation stage (*A* in Fig. 6, 1.53 h. after the beginning of the test); **b** at the end of the uniform deformation stage (*B* in Fig. 6, 6.38 h. after the beginning of the test); and **c** at the end of the accelerated deformation stage (*C* in Fig. 6, 8.52 h. after the beginning of the test)



(a) Velocity vectors and surface deformation at the end of the initial deformation stage.



(b) Velocity vectors and surface deformation at the end of the uniform deformation stage.



(c) Velocity vectors and surface deformation at the end of the accelerated deformation stage.

displacements were uniform and oriented in the same direction, from the crest toward the toe. In addition, the deformation occurred primarily at the back of the model. No cracks were observed on the surface during this stage (refer to the inset in Fig. 7a).

During the uniform deformation stage (485.22–1,367.93 N; 1.53–6.38 h), the velocity vectors began to show a more pronounced horizontal component. Large velocities were concentrated at the location of the crack (dashed line in Fig. 7b). These changes were accompanied with the development and propagation of stress-release cracks on the surface (dashed line in the inset in Fig. 7b).

During the accelerated deformation stage, the displacement vectors were concentrated near the landslide toe area (dashed line in Fig. 7c). Failure occurred in the form of cracks that were perpendicular to the main sliding direction (dashed line in the inset of Fig. 7c).

The soil formed a homogeneous pattern at the back of the model during the initial deformation stage. The displacement vectors subsequently changed to a pattern that was concentrated in the crack zone during the uniform deformation stage. As the load progressively increased, the displacement vectors concentrated at the toe of the landslide.

The evaluation of the horizontal force (horizontal soil pressure) and its distribution is a necessary input for the design of the support or for the stabilization of landslides (Zhou et al. 2014; Mei et al. 2009; Zhang et al. 1998). The conventional limit equilibrium method (LEM) has been extensively employed to evaluate the lateral force that acts on support devices, such as piles (successfully employed to stabilize landslides in the Three Gorges Reservoir, e.g., Zhou et al. 2014). Standard practice involves calculation of the lateral force using the LEM and assuming a particular distribution of the force with depth, which has traditionally been assumed to be rectangular, trapezoidal, triangular, or parabolic (Zhou et al. 2014). However, this assumption does not consider how the distribution evolves with landslide displacements.

The soil pressure distribution during the initial deformation stage (0–485.22 N) is shown in Fig. 8. The soil pressure with depth at the top of the slope (at PC1) and at the middle of the slope (at PC2) are depicted in Fig. 8b and c, respectively. The applied load is shown in Fig. 8a. The spatial distribution of the soil pressure was obtained by interpolation of the data from the PCs (Fig. 8d). Figure 8b, c shows that the soil pressure with depth can be approximated with a rectangular distribution due to the uniform readings that are obtained with depth. Figure 8b, c shows that the maximum soil pressures occurred at the surface (0.20 kPa at PC1–1 and 0.22 kPa at PC2–2). Note that the maximum soil pressure was located at the point where the surface changed slope (Fig. 8d).

The uniform deformation stage includes the load range from 485 N to 1368 N. In the upslope region (Fig. 9b) at a load of 1250 N (5.80 h; Fig. 9a), the pressure distribution was trapezoidal. The maximum pressure of 2.22 kPa occurred at a depth of 18 cm (PC1–4; Fig. 9b, d). In the middle region, the shape of the pressure distribution was also trapezoidal, and the maximum pressure (1.59 kPa at PC2–3) was located 15 cm below the surface (Fig. 9c, d).

When an applied load of 1368 N was attained, the landslide model entered the accelerated deformation stage, which has an upper bound of a 1873 N load. When an applied load of 1650 N was attained (8.00 h; Fig. 10a), the soil pressure distribution in the upslope region was parabolic with a maximum value of 3.07 kPa at a depth of 24 cm (PC1–4; Fig. 10b, d). The maximum pressure remained unchanged from the uniform deformation stage. The soil pressure distribution in the middle slope region was also parabolic with a maximum value of 1.83 kPa at PC 2–3; i.e., at a depth of 20 cm (Fig. 10b, d). In this stage, the maximum soil pressure moved from 15 cm below the surface in the previous stage to 20 cm below the surface.

The model results indicate that the lateral force along a vertical profile is not constant but significantly changes during landslide evolution. The lateral force had a rectangular vertical profile during the initial deformation and became trapezoidal, and subsequently parabolic, during the uniform deformation stage and accelerated deformation stage, respectively. The depth of the maximum soil pressure generally increased with loading.

The infrared radiation (IRR) imager captured and recorded thermal images of the model surface. A small study area (19 × 24.3 cm; refer to Figs. 4 and 11) was selected. The parameter Δ IRR, which is the change of the infrared radiation with time/load, was used to monitor changes in surface temperature during the test. The Δ IRR results and histograms of Δ IRR during the test are shown in Figs. 11, 12 and 13. The change in surface temperature was mapped to a blue-to-red rainbow color gradient. Two monitoring circles—Tc1 and Tc2—with locations shown in Figs. 11, 12 and 13, were selected from the thermal image. The monitoring circle Tc1 was located on the landslide area immediately above the toe of the landslide, and monitoring circle Tc2 was located outside the landslide area. The surface displacements are also shown in Figs. 11, 12 and 13. Figure 14 displays a plot of the average change in temperature (Δ AIRT) and the room temperature, which was constant during the test.

During the initial deformation stage (O–A in Fig. 14) Δ AIRT was very small. During the uniform deformation stage (the A–B segment in Fig. 14) the Δ AIRT displays step-like increases at the two monitoring circles. The Δ AIRT values at Tc1 and Tc2 were approximately equivalent until 3.3 h from the beginning of the test. With

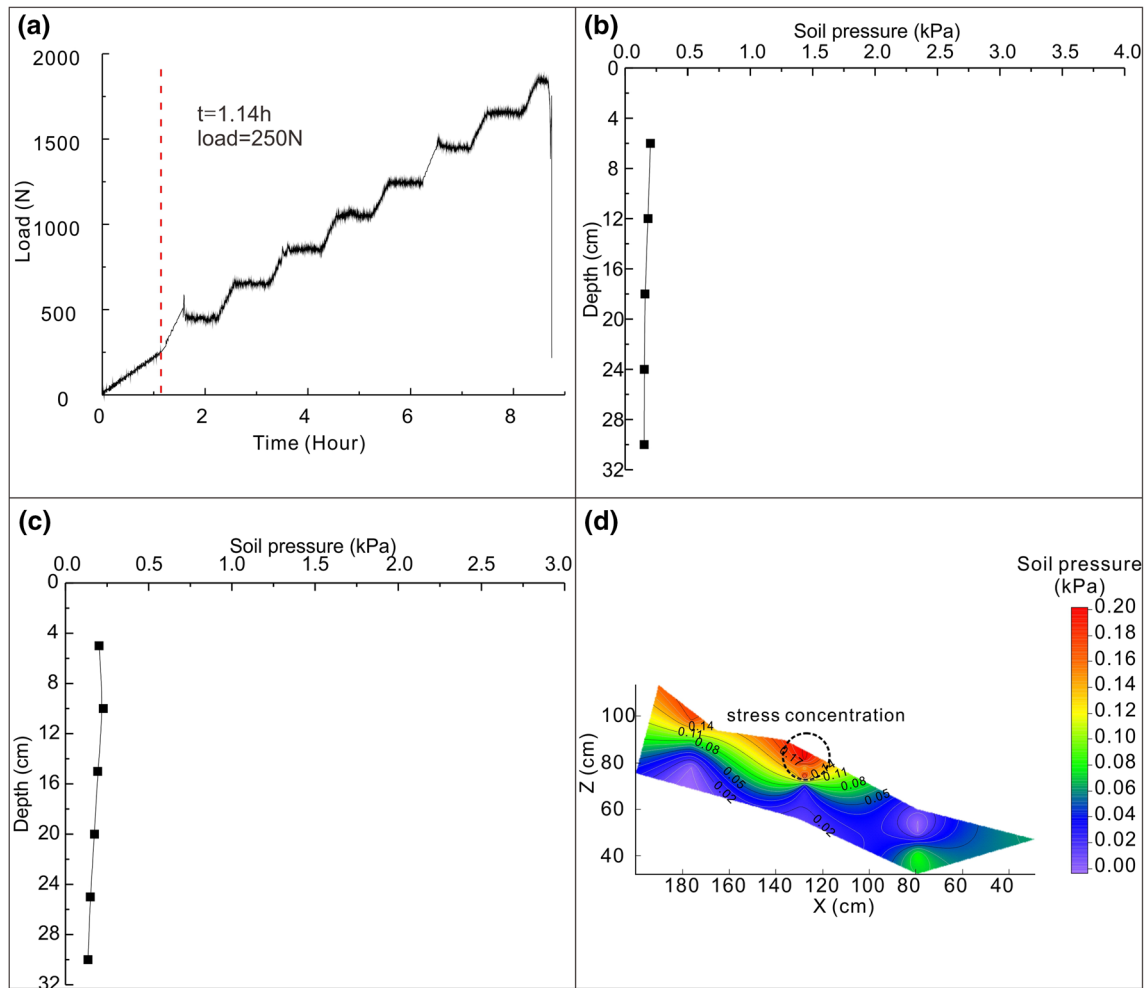


Fig. 8 Stress distribution during the initial deformation stage. **a** Applied load (time = 1.14 h; load = 250 N). **b** Soil pressure with depth at the top of the slope (PC1). **c** Soil pressure distribution in the middle (PC2). **d** Spatial distribution of the soil pressure

increased loading, the surface temperature at Tc1 became larger than the surface temperature at Tc2. To a load of 45.5 % of the peak (852.3 N; 4.25 h), no significant displacements occurred within the area of thermal monitoring (Fig. 11a). During this stage, the thermal image displayed a small but distinct average temperature increase of 0.382 °C (Fig. 11b, c) with a standard deviation of $\sigma_a = 0.094$ °C. The temperature histogram shows that the surface temperature increase conformed to a normal distribution (Fig. 11c). At the end of this stage, a temperature difference between Tc1 and Tc2 of 0.24 °C was attained.

After the slip surface formed at 6.38 h, the landslide entered the accelerated deformation stage (*B–C* segment in Fig. 14). The Δ AIRT curve on the landslide area (Tc1) decreased after a short period of rapid growth (Fig. 14). This finding is consistent with observations from previous observations in rock (Wu et al. 2006b), which indicated that the AIRT increased with loading but decreased slightly during rock fracturing and failure.

When an applied load of 86.0 % of the peak (1611.60 N; 7.42 h) was attained, small but distinct displacements of 4–6 cm were observed within the thermal study area (Fig. 12a). The surface temperature significantly increased; the average increase was 0.803 °C (Fig. 12b, c). The standard deviation was 0.211 for the entire thermal image, which suggests that the temperature was extensively distributed (Fig. 12c). A distinct difference in the surface temperature was observed between the landslide area and the stable area. The surface temperature in the landslide area was higher than the surface temperature in the stable area (Fig. 12b), which was likely caused by elastic–plastic deformation, surface energy, friction and heat (Wu et al. 2006a). Figure 12c shows that the surface temperature did not follow a normal distribution.

At the end of the accelerated deformation stage, when an applied force of 97.7 % of the peak (1829.57 N; 8.42 h) was attained, the displacements in the thermal study area

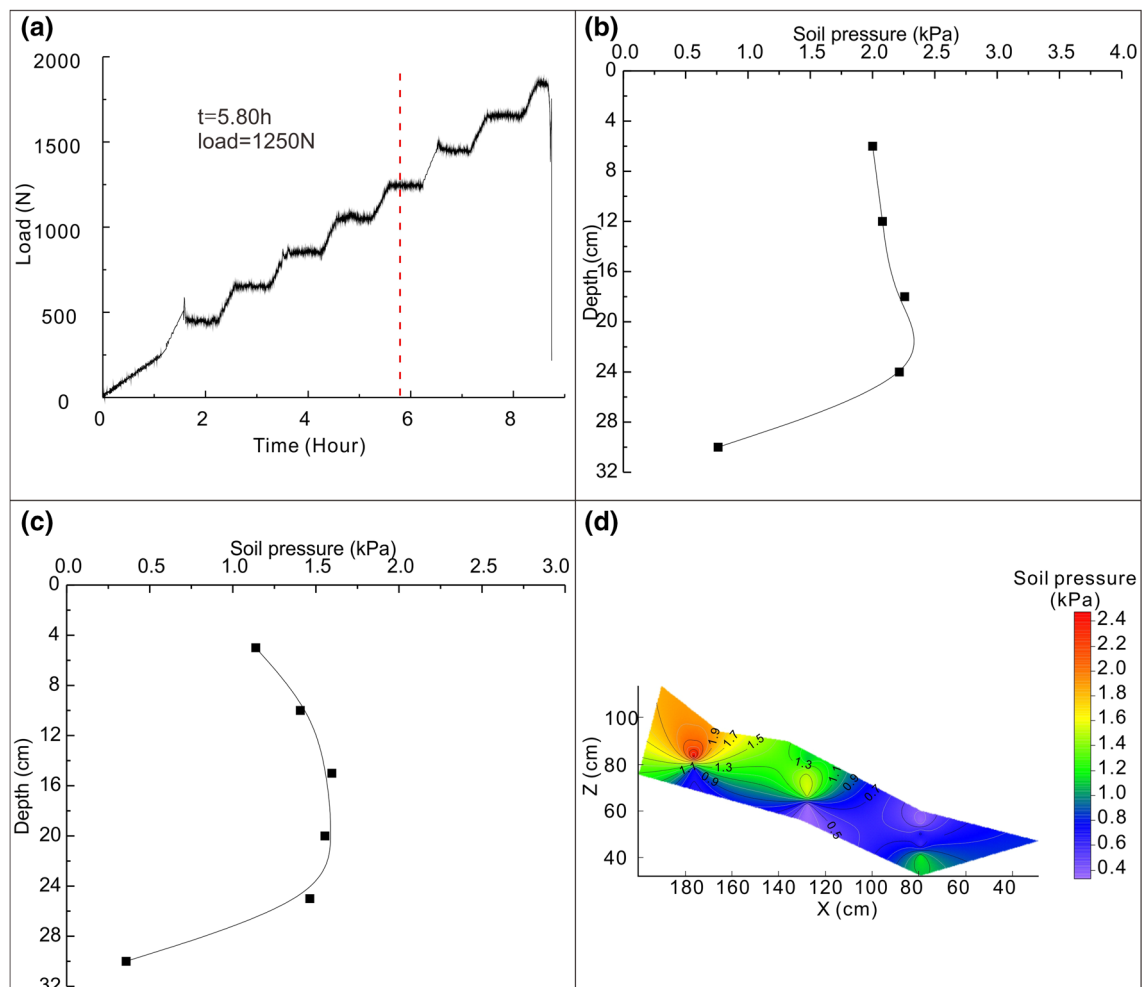


Fig. 9 Stress distribution during the uniform deformation stage. **a** Applied load (time = 5.80 h; load = 1250 N). **b** Soil pressure with depth at the top of the slope (PC1). **c** Soil pressure distribution with depth in the middle slope region (PC2). **d** Spatial distribution of the soil pressure

increased. The high standard deviation ($\sigma_c = 0.234$ °C) indicated that the difference in the change in surface temperature were further distributed (Fig. 13c). Compared with the histogram in Fig. 12c, the frequency of low temperatures (0.2–0.6 °C) was higher than the frequency of low temperatures in the previous phase (Fig. 13c). The average temperature in the thermal image decreased to 0.751 °C. The experimental results indicate that the surface temperature decreased prior to landslide failure. The decrease in surface temperature was likely caused by energy dissipation (Wu et al. 2006a) from the model slope.

These results indicate that the surface temperature in the landslide area is higher than the temperature in the stable area. This finding can potentially be used as an indicator for landslide detection. Prior to landslide failure, the average change in IRR temperature ($\Delta AIRT$) in the landslide area significantly increases and subsequently decreases.

Discussion and conclusions

In this study, a 1 g model test was performed to investigate the temporal-spatial evolution of landslide failure. A multiple monitoring system that consisted of a 3D laser scanner, PIV imager, soil PCs and thermal imaging was designed and implemented in the model to characterize the deformation, lateral soil pressure and surface temperature evolution during slip. The Majiagou landslide in the Three Gorges reservoir area was used as a reference to develop the laboratory model. The objective of the study was to construct a credible model in the laboratory to assess the potential for area-intensive measurement systems and relate observations with landslide movement and failure. The scope of the study did not involve duplicating or reproducing field observations.

In the model test, a step-like deformation behavior was reproduced. Many landslides in the Three Gorges reservoir

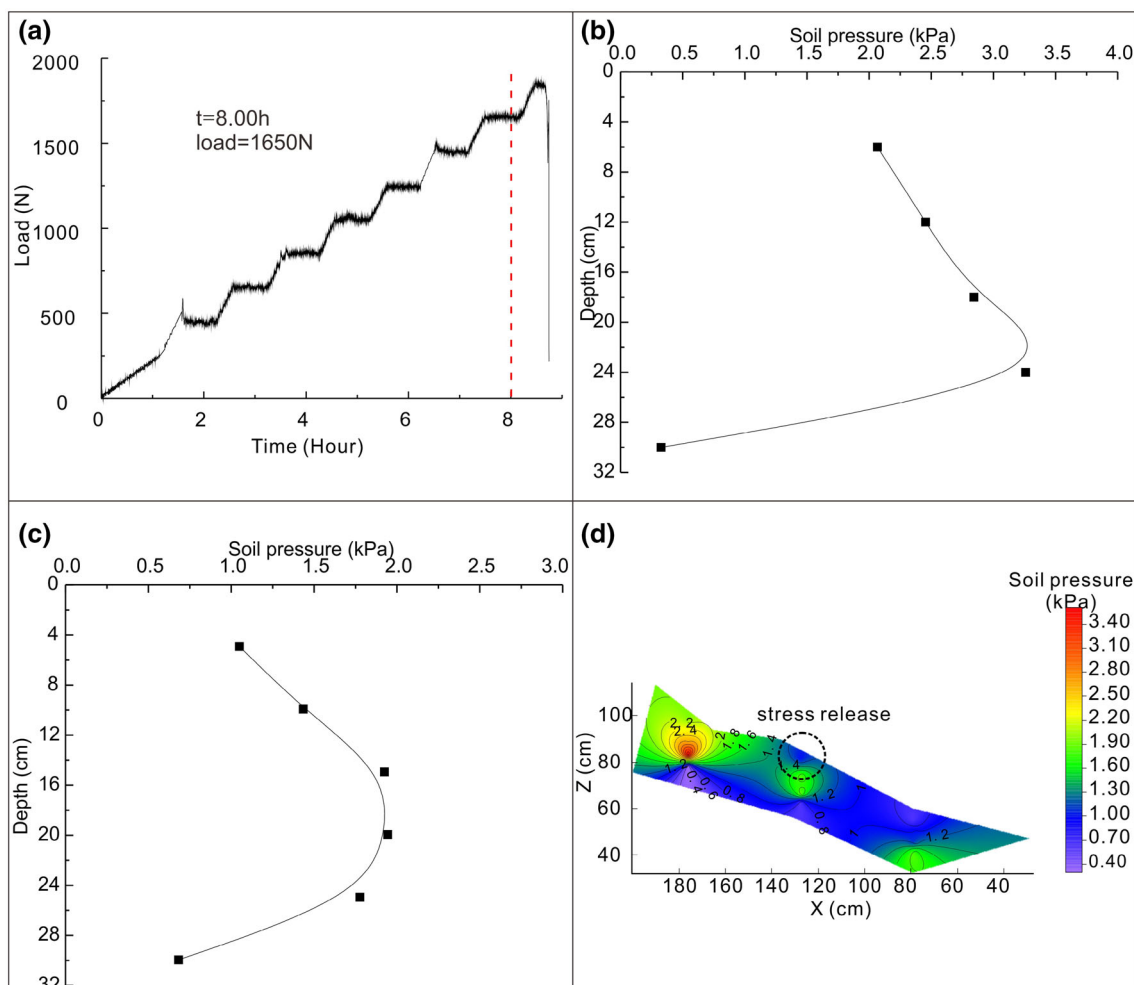


Fig. 10 Stress distribution during the accelerated deformation stage. **a** Applied load (time = 8.00 h; load = 1650 N). **b** Soil pressure with depth at the top of the slope (PC1). **c** Soil pressure distribution with depth in the middle slope region (PC2). **d** Spatial distribution of the soil pressure

area exhibit step-like deformation behavior due to the periodic fluctuations in water level (Cao et al. 2015; Li et al. 2009, 2010; Li and Yin 2011). The displacement in the model test appeared to reasonably reflect the behavior of the prototype landslide under periodic water level fluctuation conditions compared with the field observations of landslide deformation in the Three Gorges reservoir area. The preliminary results suggest that the surface temperature can potentially be used as an indicator for landslide detection.

Based on this study, the initiation of landslide model failure can be identified from PIV image analysis where local displacements were observed at the toe crack of the landslide. This finding is consistent with observations from other model tests (Wang and Lin 2011) that showed that the initiation and failure of landslides can be defined from PIV image analysis of the crack development where local displacements were observed.

The soil pressure distributions of the prototype landslide—the Majiagou landslide (Fig. 15)—show that the lateral force along a vertical profile is not constant but changes significantly with landslide deformation. The soil pressure with depth can be approximated with a rectangular distribution during the initial deformation (Fig. 15a) and become parabolic with a landslide displacement increment (Fig. 15b). This finding is consistent with the results from the model test. The present results show that it is hardly unreasonable to ignore how the distribution of the horizontal fore evolves with landslide displacement. An optimal design of the support or for the stabilization of landslide should be based on the observed data that define the evolution stage. For slide masses in the initial deformation stage, assume the lateral fore as rectangular; for slide masses in the uniform deformation stage and accelerated deformation stage, assume the lateral force as trapezoidal and subsequently parabolic, respectively.

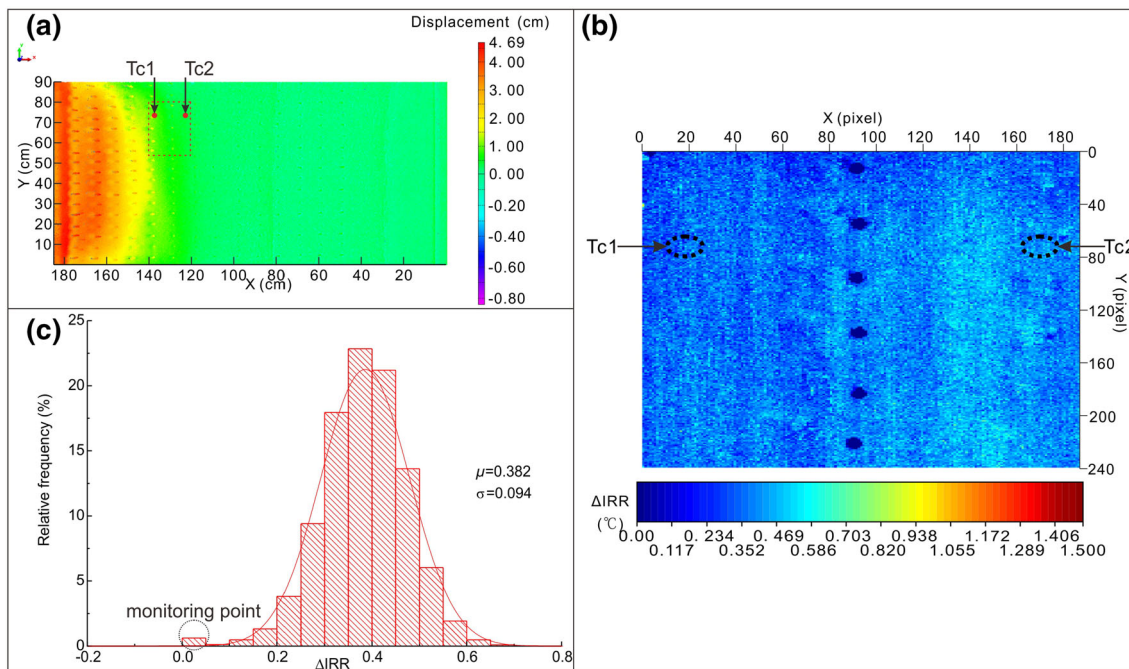


Fig. 11 **a** Surface displacements during the uniform deformation stage (852.3 N; 45.5 % of the peak). **b** Spatial distribution of the change in temperature. **c** Histogram of the change in surface temperature (the average value is $\mu_a = 0.382$ °C, and the standard deviation is $\sigma_a = 0.094$ °C)

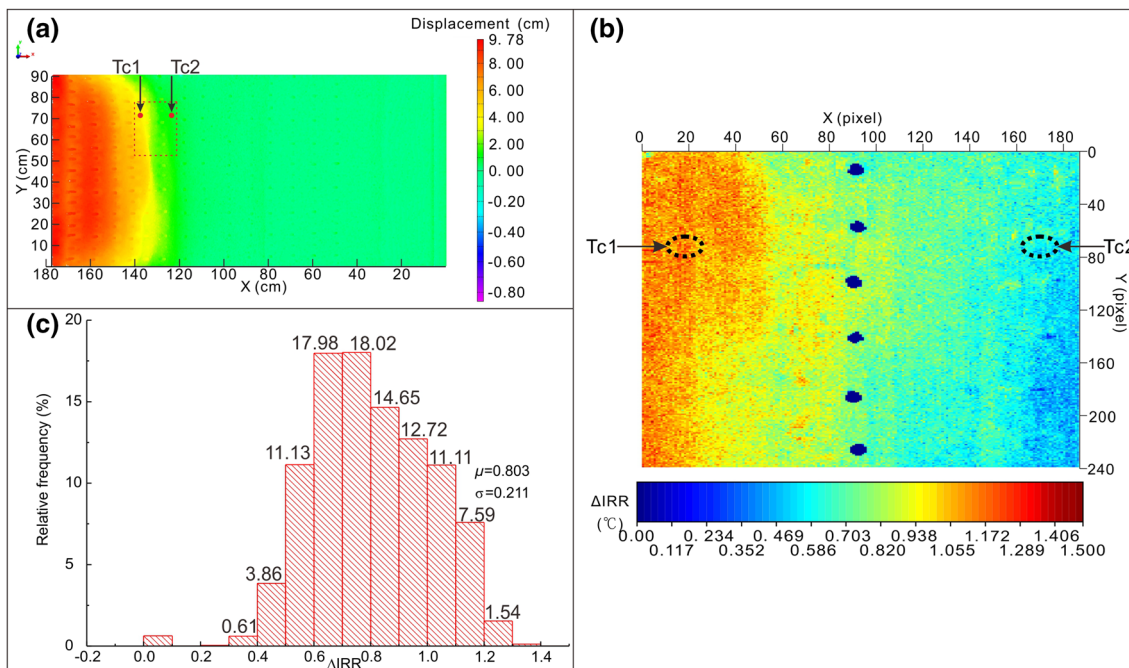


Fig. 12 **a** Surface displacements during the accelerated deformation stage (1611.60 N; 86.0 % of the peak). **b** Spatial distribution of the change in temperature. **c** Histogram of the change in surface temperature ($\mu_b = 0.803$ °C; $\sigma_b = 0.211$ °C)

The model results indicate that the surface temperature in the landslide area was higher than the surface temperature outside the unstable area. This finding is consistent with previous field observations (Kusaka et al. 1993;

Shikada et al. 1994), which reveal that the surface temperature in landslide areas is higher than the surface temperature in non-landslide areas.

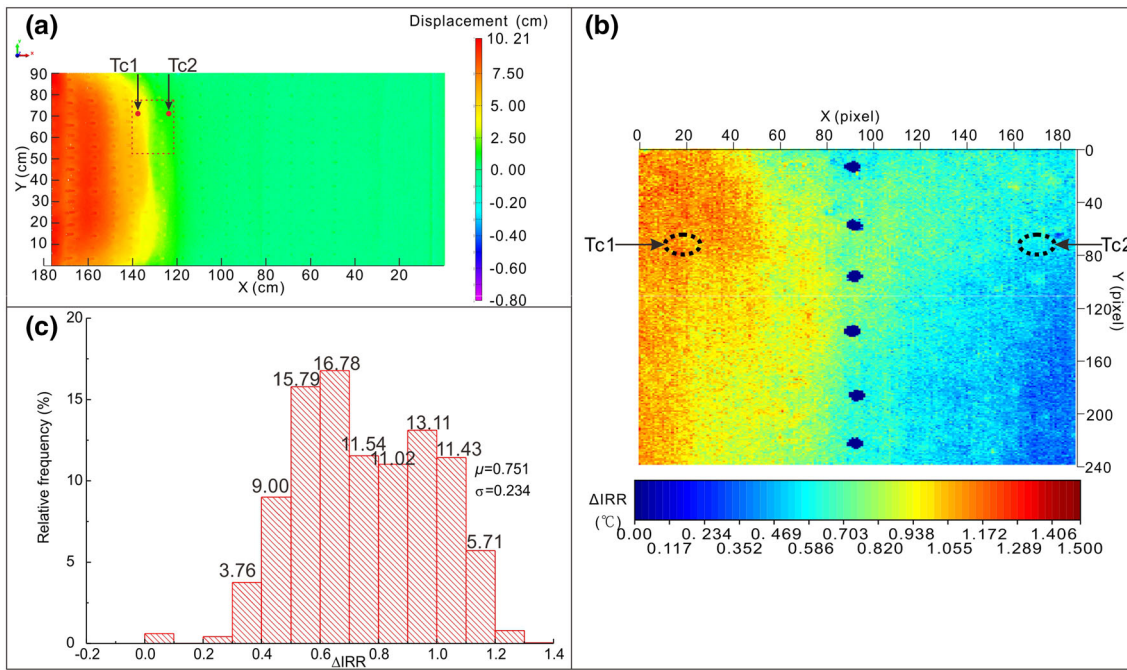
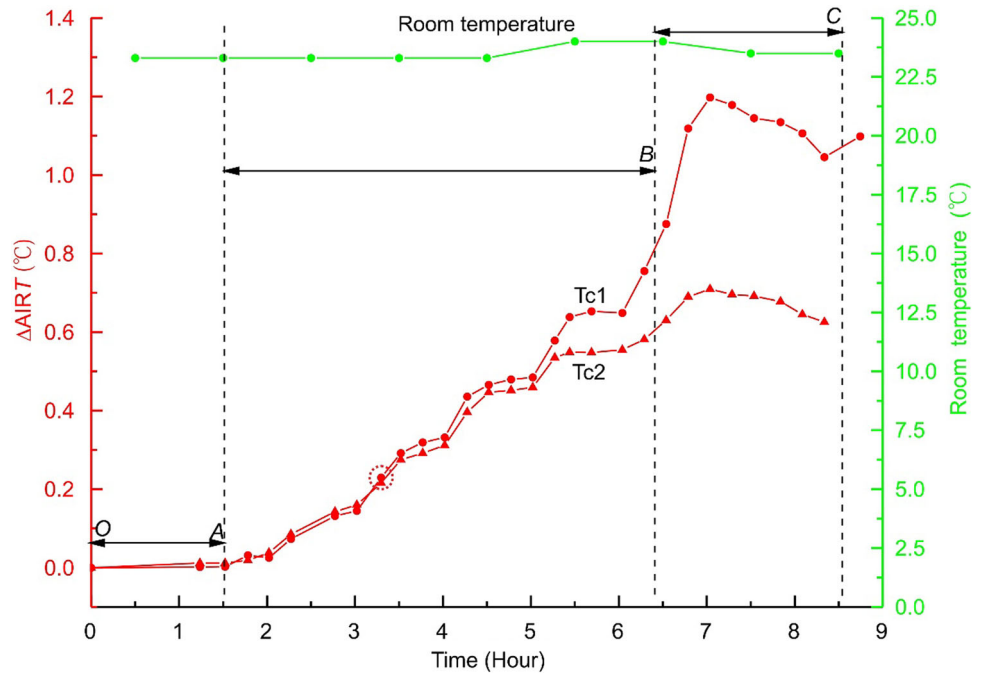


Fig. 13 **a** Surface displacements during the accelerated deformation stage (1829.57 N; 97.7 % of the peak). **b** Spatial distribution of change in temperature. **c** Histogram of the change in surface temperature ($\mu_c = 0.751$ °C, $\sigma_c = 0.234$ °C)

Fig. 14 Average changes in temperature ($\Delta AIRT$) measured at monitoring circles Tc1 and Tc2 and room temperature during the test (the locations of the monitoring circles are shown in Figs. 11, 12 and 13). Section *OA* denotes the initial deformation stage; section *AB* denotes the uniform deformation stage, and the accelerated deformation stage is represented by section *BC*



These results indicate that the observations of the model test appeared to reasonably reflect the behavior of the prototype landslide failure compared with field observations and other model tests. The following conclusions from the study were obtained:

1. The entire landslide movement was successfully recorded by the multiple monitoring system, which enabled a qualitative interpretation of the spatial-temporal evolution of the landslide failure. The positive results demonstrate that the novel monitoring

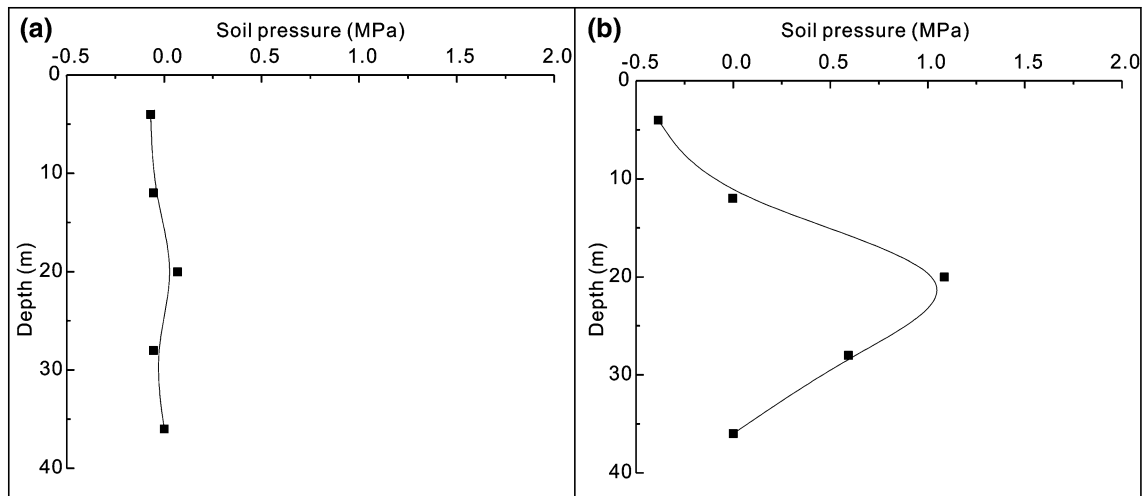


Fig. 15 Lateral force along a vertical profile of the prototype landslide—the Majiagou landslide—for the period from November 2012 to September 2013. **a** November 2012; **b** September 2013

system can prove useful to determine the initiation of sliding and to detect the mass movement and landslide area.

- Four stages of evolution, namely, initial, uniform, accelerated and failure, were identified based on the observed displacements.
- The soil movement exhibited a homogeneous velocity pattern at the rear of the model during the initial deformation stage. During the uniform deformation stage, displacements concentrated within the crack zone that formed as the load increased. With additional loading, the landslide entered the accelerated deformation stage, in which the displacements were concentrated near the landslide toe.
- The horizontal soil pressures showed that the soil stresses along a vertical profile were not constant but changed during landslide deformation. The depth of the maximum soil pressure increased with landslide movement.
- The surface temperature in the landslide area was significantly higher than the surface temperature outside the unstable area. This observation may be used as an index for identifying landslide areas. The average change in surface temperature ($\Delta AIRT$) within the unstable area significantly increased and subsequently decreased prior to failure.

Acknowledgments Junwei Ma is grateful to the China Scholarship Council for providing a scholarship for this research, which was conducted while he served as a Visiting Research Scholar at Purdue University. This study was financially supported by the National Basic Research Program “973” Project of the Ministry of Science and the Technology of the People’s Republic of China (2011CB710604 & 2011CB710606), the Key National Natural Science Foundation of China (41230637), National Natural Science Foundation of China

(41572279, 41272305 and 41102195), China Postdoctoral Science Foundation (Grant Nos. 2012M521500 and 2014T70758), and Hubei Provincial Natural Science Foundation of China (Grant No. 2014CFB901). All support is gratefully acknowledged.

References

- Abellán A, Vilaplana JM, Martínez J (2006) Application of a long-range terrestrial laser scanner to a detailed rockfall study at Vall de Núria (Eastern Pyrenees, Spain). *Eng Geol* 88:136–148. doi:10.1016/j.enggeo.2006.09.012
- Abellán A, Vilaplana JM, Calvet J, Blanchard J (2010) Detection and spatial prediction of rockfalls by means of terrestrial laser scanner monitoring. *Geomorphology* 119:162–171. doi:10.1016/j.geomorph.2010.03.016
- Angeli MG, Pasuto A, Silvano S (2000) A critical review of landslide monitoring experiences. *Eng Geol* 55(3):133–147. doi:10.1016/S0013-7952(99)00122-2
- Baba HO, Peth S (2012) Large scale soil box test to investigate soil deformation and creep movement on slopes by particle image velocimetry (PIV). *Soil Tillage Res* 125:38–43. doi:10.1016/j.still.2012.05.021
- Bridgman PW (1922) *Dimensional analysis*. Yale University Press, New Haven
- Cao Y, Yin KL, Alexander D, Zhou C (2015) Using an extreme learning machine to predict the displacement of step-like landslides in relation to controlling factors. *Landslides*. doi:10.1007/s10346-015-0596-z
- Casagli N, Catani F, Del Ventisette C, Luzi G (2010) Monitoring, prediction, and early warning using ground-based radar interferometry. *Landslides* 7(3):291–301. doi:10.1007/s10346-010-0215-y
- Casson B, Delacourt C, Baratoux D, Allemand P (2003) Seventeen years of the “La Clapière” landslide evolution analysed from ortho-rectified aerial photographs. *Eng Geol* 68(1–2):123–139. doi:10.1016/s0013-7952(02)00201-6
- Cheng SG, Luo XQ (2010) Research on theory and application of landslide model test. *J Coal Sci Eng (China)* 16:140–143
- Corominas J, Moya J, Lloret A, Gili JA, Angeli MG, Pasuto A (2000) Measurement of landslide displacements using a wire extensometer. *Eng Geol* 55:149–166

- Corsini A, Pasuto M, Soldati A, Zannoni A (2005) Field monitoring of the Corvara landslide (Dolomites, Italy) and its relevance for hazard assessment. *Geomorphology* 66(1–4):149–165
- De Bruyn D, Thimus JF (1996) The influence of temperature on mechanical characteristics of Boom clay: the results of an initial laboratory programme. *Eng Geol* 41(1–4):117–126. doi:10.1016/0013-7952(95)00029-1
- Fan XM, Xu Q, Zhang ZY, Meng DS, Tang R (2009) The genetic mechanism of a translational landslide. *Bull Eng Geol Environ* 68:231–244
- Fanti R, Gigli G, Lombardi L, Tapete D, Canuti P (2013) Terrestrial laser scanning for rockfall stability analysis in the cultural heritage site of Pitigliano (Italy). *Landslides* 10:409–420. doi:10.1007/s10346-012-0329-5
- Feng B, Wang JX, Tian PZ, Si PF (2015) Experimental study on rainfall-induced three-dimensional deformation characteristics of a slope. *Adv Mater Res* 1065–1069:133–137. doi:10.4028/www.scientific.net/AMR.1065-1069.133
- Gischig VS, Moore JR, Evans KF, Amann F, Loew S (2011a) Thermomechanical forcing of deep rock slope deformation: 1. Conceptual study of a simplified slope. *J Geophys Res Earth Surf* 116:FO4010. doi:10.1029/2011JF002006
- Gischig VS, Moore JR, Evans KF, Amann F, Loew S (2011b) Thermomechanical forcing of deep rock slope deformation: 2. The Randa rock slope instability. *J Geophys Res Earth Surf* 116:FO4011. doi:10.1029/2011JF002007
- Gokceoglu C, Sezer E (2009) A statistical assessment on international landslide literature (1945–2008). *Landslides* 6:345–351. doi:10.1007/s10346-009-0166-3
- Iai S (1989) Similitude for shaking table tests on soil-structure-fluid model in 1-g gravitational field. *Soils Found* 29(1):105–118. doi:10.3208/sandf1972.29.105
- Iverson RM (2015) Scaling and design of landslide and debris-flow experiments. *Geomorphology* 244:9–20. doi:10.1016/j.geomorph.2015.02.033
- Jaboyedoff M, Oppikofer T, Abellán A, Derron MH, Loye A, Metzger R, Pedrazzini A (2012) Use of LIDAR in landslide investigations: a review. *Nat Hazards* 61(1):5–28. doi:10.1007/s11069-010-9634-2
- Jia GW, Zhan TLT, Chen YM, Fredlund DG (2009) Performance of a large-scale slope model subjected to rising and lowering water levels. *Eng Geol* 106:92–103. doi:10.1016/j.enggeo.2009.03.003
- Kusaka T, Shikada M-a, Kawata Y (1993) Inference of landslide areas using spatial features and surface temperature of watersheds. *SPIE International Symposium on Optical Engineering and Photonics Aerospace and Remote Sensing*, pp 241–246
- Li DY, Yin KL (2011) Deformation characteristics of landslide with step-like deformation in the Three Gorges Reservoir. In: *Electric technology and civil engineering (ICETCE 2011)*, pp 6517–6520. doi:10.1109/ICETCE.2011.5774665
- Li CD, Tang HM, Hu XL, Li DM, Hu B (2009) Landslide prediction based on wavelet analysis and cusp catastrophe. *J Earth Sci China* 20:971–977. doi:10.1007/s12583-009-0082-4
- Li DY, Yin KL, Leo C (2010) Analysis of Baishuihe landslide influenced by the effects of reservoir water and rainfall. *Environ Earth Sci* 60:677–687. doi:10.1007/s12665-009-0206-2
- Lin ML, Wang KL (2006) Seismic slope behavior in a large-scale shaking table model test. *Eng Geol* 86:118–133. doi:10.1016/j.enggeo.2006.02.011
- Liu YR, Guan FH, Yang Q, Yang RQ, Zhou WY (2013) Geomechanical model test for stability analysis of high arch dam based on small blocks masonry technique. *Int J Rock Mech Min* 61:231–243. doi:10.1016/j.ijrmms.2013.03.003
- Luo XQ, Sun H, Tham LG, Junaideen SM (2010) Landslide model test system and its application on the study of Shiliushubao landslide in Three Gorges Reservoir area. *Soils Found* 50:309–317. doi:10.3208/sandf.50.309
- Ma JW, Tang HM, Hu XL, Bobet Antonio, Zhang M, Zhu TW, Song YJ, Eldin Ez, Mutasim AM (2016) Identification of causal factors for the Majiagou landslide using modern data mining methods. *Landslides*. doi:10.1007/s10346-016-0693-7
- Mei GX, Chen QM, Song LH (2009) Model for predicting displacement-dependent lateral earth pressure. *Can Geotech J* 46(8):969–975. doi:10.1139/T09-040
- Moriwaki H, Inokuchi T, Hattajji T, Sassa K, Ochiai H, Wang G (2004) Failure processes in a full-scale landslide experiment using a rainfall simulator. *Landslides* 1:277–288. doi:10.1007/s10346-004-0034-0
- Ochiai H, Okada Y, Furuya G, Okura Y, Matsui T, Sammori T, Terajima T, Sassa K (2004) A fluidized landslide on a natural slope by artificial rainfall. *Landslides* 1:211–219. doi:10.1007/s10346-004-0030-4
- Rianna G, Pagano L, Urciuoli G (2014) Rainfall patterns triggering shallow flowslides in pyroclastic soils. *Eng Geol* 174:22–35. doi:10.1016/j.enggeo.2014.03.004
- Shikada M, Kusaka T, Kawata Y, Miyakita K (1994) Extraction of characteristic properties in landslide areas using thematic map data and surface temperature. In: *International geoscience and remote sensing symposium (IGARSS), better understanding of earth environment*, vol 5, pp 103–105
- Squarzoni C, Delacourt C, Allemand P (2003) Nine years of spatial and temporal evolution of the La Valette landslide observed by SAR interferometry. *Eng Geol* 68:53–66. doi:10.1016/S0013-7952(02)00198-9
- Strozzi T, Farina P, Corsini A, Ambrosi C, Thüring M, Zilger J, Wiesmann A, Wegmüller U, Werner C (2005) Survey and monitoring of landslide displacements by means of L-band satellite SAR interferometry. *Landslides* 2:193–201. doi:10.1007/s10346-005-0003-2
- Sun YJ, Zhang D, Shi B, Tong HJ, Wei GQ, Wang X (2014) Distributed acquisition, characterization and process analysis of multi-field information in slopes. *Eng Geol* 182, Part A:49–62. doi:10.1016/j.enggeo.2014.08.025
- Tang HM, Hu XL, Xu C, Li CD, Yong R, Wang LQ (2014a) A novel approach for determining landslide pushing force based on landslide-pile interactions. *Eng Geol* 182, Part A:15–24. doi:10.1016/j.enggeo.2014.07.024
- Tang HM, Li CD, Hu XL, Su AJ, Wang LQ, Wu YP, Criss R, Xiong CR, Li YA (2014b) Evolution characteristics of the Huangtupo landslide based on in situ tunneling and monitoring. *Landslides* 12:511–521. doi:10.1007/s10346-014-0500-2
- Tarchi D, Casagli N, Fanti R et al (2003) Landslide monitoring by using ground-based SAR interferometry: an example of application to the Tessina landslide in Italy. *Eng Geol* 68:15–30. doi:10.1016/S0013-7952(02)00196-5
- Thielicke W, Stamhuis EJ (2014) PIVlab-time-resolved digital particle image velocimetry tool for MATLAB. <http://pivlab.blogspot.gr/>
- Travelletti J, Oppikofer T, Delacourt C, Malet J, Jaboyedoff M (2008) Monitoring landslide displacements during a controlled rain experiment using a long-range terrestrial laser scanning (TLS). *Int Arch Photogramm Remote Sens* 37(Part B5):485–490
- van Westen CJ, Lulie Getahun F (2003) Analyzing the evolution of the Tessina landslide using aerial photographs and digital elevation models. *Geomorphology* 54:77–89. doi:10.1016/S0169-555X(03)00057-6
- Walstra J, Chandler J, Dixon N, Dijkstra T (2004) Time for change—quantifying landslide evolution using historical aerial photographs and modern photogrammetric methods. *Int Arch Photogramm Remote Sens Spat In Sci*, vol 34 (Part XXX). Commission 4:475–481

- Wang KL, Lin ML (2011) Initiation and displacement of landslide induced by earthquake—a study of shaking table model slope test. *Eng Geol* 122:106–114. doi:[10.1016/j.enggeo.2011.04.008](https://doi.org/10.1016/j.enggeo.2011.04.008)
- Wang GQ, Joyce J, Phillips D, Shrestha R, Carter W (2013) Delineating and defining the boundaries of an active landslide in the rainforest of Puerto Rico using a combination of airborne and terrestrial LIDAR data. *Landslides* 10:503–513. doi:[10.1007/s10346-013-0400-x](https://doi.org/10.1007/s10346-013-0400-x)
- Wu LX, Cui CY, Geng NG, Wang JZ (2000) Remote sensing rock mechanics (RSRM) and associated experimental studies. *Int J Rock Mech Min* 37:879–888. doi:[10.1016/S1365-1609\(99\)00066-0](https://doi.org/10.1016/S1365-1609(99)00066-0)
- Wu LX, Liu SJ, Wu YH, Wu HP (2002) Changes in infrared radiation with rock deformation. *Int J Rock Mech Min* 39:825–831. doi:[10.1016/S1365-1609\(02\)00049-7](https://doi.org/10.1016/S1365-1609(02)00049-7)
- Wu LX, Liu SJ, Wu YH, Wang CY (2006a) Precursors for rock fracturing and failure—Part I: IRR image abnormalities. *Int J Rock Mech Min* 43:473–482. doi:[10.1016/j.ijrmms.2005.09.002](https://doi.org/10.1016/j.ijrmms.2005.09.002)
- Wu LX, Liu SJ, Wu YH, Wang CY (2006b) Precursors for rock fracturing and failure—Part II: IRR T-Curve abnormalities. *Int J Rock Mech Min* 43:483–493. doi:[10.1016/j.ijrmms.2005.09.001](https://doi.org/10.1016/j.ijrmms.2005.09.001)
- Zhang Z, Luo X, Wu J (2009) Study on the possible failure mode and mechanism of the Xietan landslide when exposed to water level fluctuation. In: Wang F, Li T (eds) *Landslide disaster mitigation in Three Gorges Reservoir*. Environmental Science and Engineering. Springer, Berlin, pp 375–385. doi:[10.1007/978-3-642-00132-1_16](https://doi.org/10.1007/978-3-642-00132-1_16)
- Zhang JM, Shamoto Y, Tokimatsu K (1998) Evaluation of earth pressure under any lateral deformation. *Soils Found* 38:15–33. doi:[10.3208/sandf.38.15](https://doi.org/10.3208/sandf.38.15)
- Zhou CM, Shao W, van Westen CJ (2014) Comparing two methods to estimate lateral force acting on stabilizing piles for a landslide in the Three Gorges Reservoir, China. *Eng Geol* 173:41–53. doi:[10.1016/j.enggeo.2014.02.004](https://doi.org/10.1016/j.enggeo.2014.02.004)